AIAA JOURNAL
Vol. 41, No. 3, March 2003

Initial-Value Problem for Hypersonic Boundary-Layer Flows

Alexander Fedorov*
Moscow Institute of Physics and Technology, Moscow Region, 140180 Zhukovski, Russia
and
Anatoli Tumin†
University of Arizona, Tucson, Arizona 85721

An initial-value problem is analyzed for a two-dimensional wave packet induced by a local two-dimensional disturbance in a hypersonic boundary layer. The problem is solved using Fourier transform with respect to the streamwise coordinate and Laplace transform with respect to time. The temporal continuous spectrum is revisited, and the uncertainty associated with the overlapping of continuous-spectrum branches is resolved. It is shown that the discrete spectrum's dispersion relationship is nonanalytic because of the synchronization of the first mode with the vorticity/entropy waves of the continuous spectrum. However, the inverse Laplace transform is regular at the synchronism point. Characteristics of the wave packet generated by an initial temperature spot are numerically calculated. It is shown that the hypersonic boundary layer is highly receptive to vorticity/entropy disturbances in the synchronism region. The feasibility of experimental verification of this receptivity mechanism is discussed.

Nomenclature

$\boldsymbol{A}$	=	vector function of six components
A_j	=	jth component of vector $\boldsymbol{A}$
D	=	d/dy
e	=	ratio of the bulk viscosity to the dynamic viscosity
H^{ij}, L^{ij}	=	ijth matrix element
M	=	Mach number
m	=	$2(e-1)/3$
P_s	=	mean pressure
Pr	=	Prandtl number
p	=	Laplace variable
Re	=	Reynolds number
r	=	$2(e+2)/3$
T	=	mean-flow temperature
t	=	time
U	=	mean-flow velocity
u	=	streamwise velocity disturbance
v	=	normal velocity disturbance
x	=	streamwise coordinate
y	=	coordinate normal to the wall
α	=	streamwise wave number
γ	=	specific heat ratio
θ	=	temperature disturbance
μ	=	viscosity disturbance
μ_s	=	mean-flow viscosity
μ'_s	=	dμ_s/dT_s
π	=	pressure disturbance
ρ	=	density disturbance
ρ_s	=	mean-flow density

Subscripts

e	=	upper boundary-layeredge
p	=	Laplace transform
s	=	mean flow
α	=	Fourier transform
*	=	synchronization

Superscripts

T	=	transposed
*	=	dimensional

Presented as Paper 2001-2781 at the AIAA 31st Fluid Dynamics Conference, Anaheim, CA, 11–14 June 2001; received 6 February 2002; revision received 1 September 2002; accepted for publication 24 October 2002.

*Associate Professor, Faculty of Aeromechanics and Flight Techniques; fedorov@falt.deep.ru. Member AIAA.

†Assistant Professor, Department of Aerospace and Mechanical Engineering; tumin@engr.arizona.edu. Senior Member AIAA.

Introduction

STUDIES of laminar-turbulent transition in hypersonic boundary-layer flows have a long history. Nevertheless, our understanding of this phenomenon is still very poor compared to the low-speed case.[1] There are several reasons for this gap. For example, experimental conditions are severe in hypersonic wind tunnels. Because of very high levels of freestream noise, it is difficult to perform experiments with controlled disturbances. It is also difficult to design perturbers providing high-frequency artificial disturbances of well-controlled characteristics. Usually experimentalists deal with wave trains or wave packets internalized in the boundary layer. Furthermore, interpretation of experimental data is not straightforward because of the complexity of receptivity and stability processes at hypersonic regimes. This issue leads to the necessity of close coordination between theoretical modeling and experimental design and testing.

A high-Reynolds-number Mach-6 quiet Ludwieg tube is under development at Purdue University.[2,3] Experiments with controlled disturbances in this facility could provide a breakthrough in experimental modeling and a detailed examination of the governing mechanisms associated with hypersonic laminar-turbulent transition. The test section of the tube will be well suited to experiments with bodies of revolution, and a sharp cone would be considered as a good candidate for transition studies because of its relatively simple mean flow. This wind tunnel will provide high Mach numbers in combination with high Reynolds numbers. Because, under these conditions, the second instability mode becomes dominant in the transition process,[4] issues related to this instability mode must be revisited.

The second-mode instability was observed in the experiments of Kendall,[5] Demitriadis,[6] Stetson et al.,[7] and Stetson and Kimmel.[8] Mach-8 stability and transition experiments[7] for the boundary layer on a sharp cone indicated that the unstable high-frequency second mode plays a major role in the conical boundary-layer transition. These data are consistent with the stability calculations,[4,9,10] which show that two-dimensional waves of the second mode have a growth rate higher than that of three-dimensional waves. To address the two-dimensional nature of the second mode, one should look

for an experimental setup providing excitation of predominantly two-dimensional disturbances.

Several methods for excitation of artificial disturbances in a hypersonic boundary layer are available. A glow discharge technique is used in the design of two-dimensional[11,12] and three-dimensional[12–14] perturbers generating disturbances at the boundary-layer bottom. They can also be used for excitation of high-frequency acoustic disturbances.[12] In Ref. 15 a laser is used to induce local disturbances in a freestream. A relatively small region of heated air is generated in front of the cone tip. The temperature spot propagates downstream and translates into a ring embracing the cone surface. The laser perturber can provide both wave trains of fixed frequency and local wave packets of a broad frequency band. This method might serve for experimental studies of the interaction between two-dimensional freestream disturbances and the boundary-layer flow. Such experiments should be accompanied by theoretical modeling in all phases, from the design of the experimental setup to the analysis and interpretation of the data.

To meet the experimental constraints just discussed, we need to focus on the theoretical modeling of excitation and on the development of two-dimensional wave trains and/or wave packets in a conical hypersonic boundary layer. Another motivation originates from the theoretical results of Gushchin and Fedorov[16] and Fedorov and Khokhlov.[17,18] They found that the second-mode instability is associated with synchronization of the first mode with the second mode. In the synchronism region the eigenvalue spectrum splits into two branches. The asymptotic analyses[17,18] of the spectrum branching show a strong intermodal exchange caused by nonparallel effects. In accordance with the intermodal exchange rule established in Refs. 17 and 18, the first (stable) mode effectively excites the second (unstable) mode in the synchronism region. To predict the initial amplitude of the second-mode instability, one should account for excitation of both the first and second modes, despite the fact that the first mode might decay downstream.

If we exclude the high-frequency vibrations of the wall, then a major source of the instability excitation is associated with the freestream disturbances. Theoretical studies[17,19] showed that the first and second modes are synchronized with acoustic waves near the leading edge of a flat plate (or near the sharp cone tip). The latter agrees with experimental observations by Chen et al.[20] that this synchronization might lead to an early transition to turbulence of the discrete modes by the freestream acoustic noise. Fedorov and Khokhlov[17,19] developed a theoretical model of this receptivity mechanism, and corresponding experimental studies were performed by Maslov et al.[12] A similar experiment with acoustic disturbances radiating the boundary layer over a sharp cone would be more complicated, as the interaction of the acoustic field with the shock wave would generate all modes of the continuous spectrum,[21] and interpretation of the data would be questionable. Another option is associated with the synchronization of a discrete mode with vorticity/entropy waves of the continuous spectra. Fedorov and Khokhlov[18] showed that the first mode (for adiabatic and weakly cooled walls) and the second mode (for strongly cooled walls) are synchronized with these freestream disturbances. The synchronization provides favorable conditions for hypersonic boundary-layer receptivity to freestream turbulence and temperature spottiness. These findings, along with the possibility of generating two-dimensional spottiness near a sharp cone model,[15] motivated the present work.

Our objective is to solve the initial-value problem for a wave packet generated by a local source, which can be a temperature spot, vortex, or a combination of the two. Because the second-mode instability is maximal for two-dimensional waves, we focus on two-dimensional disturbances propagating in a boundary layer on a sharp cone at a zero angle of attack. As the first step of this research, we consider the locally parallel approximation.

Problem Formulation

At the initial time moment $t=0$ a localized (with respect to the streaming coordinate) two-dimensional disturbance of small amplitude is internalized into a locally parallel boundary-layer flow of a calorically perfect gas. The problem is to describe the downstream evolution of this disturbance, which can be treated as a wave packet. The hydrodynamic and thermodynamic characteristics of the flow are expressed as a superposition $Q_s(y)+q(x,y,t)$, where Q_s is the mean-flow characteristic and q is its disturbance; the coordinates x, y, and time t are nondimensionalized using a length scale L^* and time L^*/U_e^*. The velocity components, temperature, and density are referenced to their quantities at the upper boundary-layer edge, and pressure is nondimensionalized using the dynamic pressure ρ_e^*/U_e^{*2}. The linearized Navier–Stokes equations for the disturbances are

$$\frac{\partial\rho}{\partial t}+\rho_s\frac{\partial u}{\partial x}+U_s\frac{\partial\rho}{\partial x}+\frac{\partial}{\partial y}(\rho_s v)=0 \tag{1a}$$

$$\rho_s\left(\frac{\partial u}{\partial t}+U_s\frac{\partial u}{\partial x}+v\frac{\partial U_s}{\partial y}\right)=-\frac{\partial\pi}{\partial x}+\frac{1}{Re}\left\{\mu_s\frac{\partial}{\partial x}\left(r\frac{\partial u}{\partial x}+m\frac{\partial v}{\partial y}\right)+\frac{\partial}{\partial y}\left[\mu_s\left(\frac{\partial u}{\partial y}+\frac{\partial v}{\partial x}\right)+\mu\frac{\partial U_s}{\partial y}\right]\right\} \tag{1b}$$

$$\rho_s\left(\frac{\partial v}{\partial t}+U_s\frac{\partial v}{\partial x}\right)=-\frac{\partial\pi}{\partial y}+\frac{1}{Re}\left\{\mu_s\frac{\partial}{\partial x}\left[\left(\frac{\partial u}{\partial y}+\frac{\partial v}{\partial x}\right)+\mu\frac{\partial U_s}{\partial y}\right]+\frac{\partial}{\partial y}\left[\mu_s\left(m\frac{\partial u}{\partial x}+r\frac{\partial v}{\partial y}\right)\right]\right\} \tag{1c}$$

$$\rho_s\left(\frac{\partial\theta}{\partial t}+U_s\frac{\partial\theta}{\partial x}+v\frac{\partial T_s}{\partial y}\right)=(\gamma-1)M_e^2\left(\frac{\partial\pi}{\partial t}+U_s\frac{\partial\pi}{\partial x}+\frac{1}{Re}\Phi\right)+\frac{1}{PrRe}\left[\mu_s\frac{\partial^2\theta}{\partial x^2}+\frac{\partial}{\partial y}\left(\mu_s\frac{\partial\theta}{\partial y}+\mu\frac{\partial T_s}{\partial y}\right)\right] \tag{1d}$$

$$\frac{\pi}{P_s}=\frac{\theta}{T_s}+\frac{\rho}{\rho_s} \tag{1e}$$

$$\Phi=\mu_s 2\left(\frac{\partial u}{\partial y}+\frac{\partial v}{\partial x}\right)\frac{\partial U_s}{\partial y}+\mu^1\left(\frac{\partial U_s}{\partial y}\right)^2 \tag{1f}$$

where $Re=\rho_e^*U_e^*L^*/\mu_e^*$ is the Reynolds number, $r=2(e+2)/3$, $m=2(e-1)/3$, and $e=0$ corresponds to the Stokes hypothesis. At this stage the mean-flow profiles $U_s(y)$ and $T_s(y)$ might be considered as a quasi-parallel approximation of an exact solution of the Navier–Stokes equations. In the present work, for the numerical implementation of the stability analysis the profiles are found from the compressible boundary-layer equations at a zero pressure gradient.

The system of equations (1a–1f) can be written for the disturbance vector function $\boldsymbol{A}=(u,\partial u/\partial y,v,\pi,\theta,\partial\theta/\partial y)^T$ in the matrix-operator form

$$\frac{\partial}{\partial y}\left(L_0\frac{\partial\boldsymbol{A}}{\partial y}\right)+\frac{\partial\boldsymbol{A}}{\partial y}=H_{10}\frac{\partial\boldsymbol{A}}{\partial t}+H_{11}\boldsymbol{A}+H_2\frac{\partial\boldsymbol{A}}{\partial x}+H_3\frac{\partial^2\boldsymbol{A}}{\partial x\partial y}+H_4\frac{\partial^2\boldsymbol{A}}{\partial x^2} \tag{2}$$

where L_0, H_{10}, H_{11}, H_2, H_3, and H_4 are 6×6 matrices. Their nonzero elements are presented in Appendix A. At the initial time moment $t=0$ the disturbance vector is specified as

$$\boldsymbol{A}(x,y,0)=\boldsymbol{A}_0(x,y) \tag{3}$$

The boundary conditions are

$$y=0: \qquad u=v=\theta=0 \tag{4a}$$

$$y\to\infty: \qquad |A_j|\to0 \qquad (j=1,\ldots,6) \tag{4b}$$

Here, Eq. (4a) corresponds to no-slip conditions and zero temperature perturbation on a wall of high thermal conductivity. Specifically, we consider the initial boundary-value problem (2–4), with the initial vector $\boldsymbol{A}_0$ of a nonzero temperature disturbance

$$A_{05}=\theta_0(x,y), \qquad A_{0j}=0 \qquad (j\neq5,6) \tag{5}$$

Formal Solution of the Initial-Value Problem

Although compressibility adds complexity to the problem, our approach is similar to the case of an incompressible boundary layer considered by Gustavsson.[22] The problem (2–4) is solved using Fourier transform with respect to x and Laplace transform with respect to t:

$$\boldsymbol{A}_{p\alpha}(y) = \frac{1}{\sqrt{2\pi}} \int_0^{\infty} e^{-pt} \int_{-\infty}^{+\infty} e^{-i\alpha x} \boldsymbol{A}(x, y, t)\, \mathrm{d}x\, \mathrm{d}t \tag{6}$$

For the amplitude vector $\boldsymbol{A}_{p\alpha}$ we obtain from Eq. (2) the nonhomogeneous system of ordinary differential equations

$$\frac{\mathrm{d}}{\mathrm{d}t}\left(L_0 \frac{\mathrm{d}\boldsymbol{A}_{p\alpha}}{\mathrm{d}y}\right) + \frac{\mathrm{d}\boldsymbol{A}_{p\alpha}}{\mathrm{d}y} = H_{10} p \boldsymbol{A}_{p\alpha} - H_{10} \boldsymbol{A}_{0\alpha}$$

$$+ H_{11} \boldsymbol{A}_{p\alpha} + i\alpha H_2 \boldsymbol{A}_{p\alpha} + i\alpha H_3 \frac{\mathrm{d}\boldsymbol{A}_{p\alpha}}{\mathrm{d}y} - \alpha^2 H_4 \boldsymbol{A}_{p\alpha} \tag{7}$$

where $\boldsymbol{A}_{0\alpha}(y)$ is a Fourier transform of the initial disturbance field $\boldsymbol{A}_0(x, y)$. The solution of Eq. (7) satisfies the boundary conditions

$$y = 0: \qquad A_{p\alpha 1} = A_{p\alpha 3} = A_{p\alpha 5} = 0 \tag{8a}$$

$$y \to \infty: \qquad |A_{p\alpha j}| \to 0 \qquad (j = 1, \ldots, 6) \tag{8b}$$

Further analysis is similar to the case of a harmonic disturbance propagating in space.[23] We begin with consideration of the homogeneous part of Eq. (7). The latter can be recast as a standard stability system of ordinary differential equations for two-dimensional compressible boundary layers:

$$\frac{\mathrm{d}\boldsymbol{A}}{\mathrm{d}y} = H_0 \boldsymbol{A} \tag{9}$$

where H_0 is a 6×6 matrix; its nonzero elements are presented in Appendix A. There are six fundamental solutions of the homogeneous system of equations: $z_1, \ldots, z_6$. Each vector function has an exponential asymptotic behavior $\exp(\lambda_j y)$ outside the boundary layer. For $y \to \infty$ the characteristic equation $\det\|H_0 - \lambda \boldsymbol{I}\| = 0$ can be written in the explicit form

$$\left(b_{11} - \lambda^2\right) \times \left[\left(b_{22} - \lambda^2\right)\left(b_{33} - \lambda^2\right) - b_{23} b_{32}\right] = 0 \tag{10}$$

where

$$b_{11} = h_0^{21}, \qquad b_{22} = H_0^{42} H_0^{24} + H_0^{43} H_0^{34} + H_0^{46} H_0^{64}$$

$$b_{23} = H_0^{42} H_0^{25} + H_0^{43} H_0^{35} + H_0^{46} H_0^{65}$$

$$b_{32} = H_0^{64}, \qquad b_{33} = H_0^{65}$$

and the elements of matrix H_0 are evaluated at $y \to \infty$. The roots of Eq. (10) are

$$\lambda_{1,2}^2 = b_{11} = \alpha^2 + iRe(\alpha - ip) \tag{11a}$$

$$\lambda_{3,4}^2 = (b_{22} + b_{33})/2 - \tfrac{1}{2}\sqrt{(b_{22} - b_{33})^2 + 4 b_{23} b_{32}} \tag{11b}$$

$$\lambda_{5,6}^2 = (b_{22} + b_{33})/2 + \tfrac{1}{2}\sqrt{(b_{22} - b_{33})^2 + 4 b_{23} b_{32}} \tag{11c}$$

For the sake of definiteness, we choose the root branches as $\mathrm{Re}(\lambda_1, \lambda_3, \lambda_5) < 0$ and introduce the matrix of fundamental solutions

$$\boldsymbol{Z} = \|z_1, \ldots, z_6\| \tag{12}$$

A solution of the nonhomogeneous system (7) is expressed in the form

$$\boldsymbol{A}_{p\alpha} = \boldsymbol{Z}\boldsymbol{Q}(y) \tag{13}$$

where the vector of coefficients $\boldsymbol{Q}$ is determined by the method of variation of the parameters:

$$2L_0 \frac{\mathrm{d}\boldsymbol{Z}}{\mathrm{d}y}\frac{\mathrm{d}\boldsymbol{Q}}{\mathrm{d}y} + L_0 \boldsymbol{Z}\frac{\mathrm{d}^2\boldsymbol{Q}}{\mathrm{d}y^2} + \frac{\mathrm{d}L_0}{\mathrm{d}y}\boldsymbol{Z}\frac{\mathrm{d}\boldsymbol{Q}}{\mathrm{d}y} + \boldsymbol{Z}\frac{\mathrm{d}\boldsymbol{Q}}{\mathrm{d}y} - i\alpha H_3 \boldsymbol{Z}\frac{\mathrm{d}\boldsymbol{Q}}{\mathrm{d}y} = \boldsymbol{F} \tag{14a}$$

$$F_j = -(H_0 \boldsymbol{A}_{0\alpha})_j \tag{14b}$$

Accounting for $\mathrm{d}\boldsymbol{Z}/\mathrm{d}y = H_0 \boldsymbol{Z}$, we obtain the system of equations

$$2L_0 H_0 \boldsymbol{Z}\frac{\mathrm{d}\boldsymbol{Q}}{\mathrm{d}y} + L_0 \boldsymbol{Z}\frac{\mathrm{d}^2\boldsymbol{Q}}{\mathrm{d}y^2} + \frac{\mathrm{d}L_0}{\mathrm{d}y}\boldsymbol{Z}\frac{\mathrm{d}\boldsymbol{Q}}{\mathrm{d}y} + \boldsymbol{Z}\frac{\mathrm{d}\boldsymbol{Q}}{\mathrm{d}y} - i\alpha H_3 \boldsymbol{Z}\frac{\mathrm{d}\boldsymbol{Q}}{\mathrm{d}y} = \boldsymbol{F} \tag{15}$$

Let us consider the fourth equation of Eq. (15)

$$2L_0^{43} z_{ij} H_0^{3i}\frac{\mathrm{d}Q_j}{\mathrm{d}y} + L_0^{43} z_{3j}\frac{\mathrm{d}^2 Q_j}{\mathrm{d}y^2} + z_{4j}\frac{\mathrm{d}Q_j}{\mathrm{d}y} + \frac{\mathrm{d}L_0^{43}}{\mathrm{d}y} z_{3j}\frac{\mathrm{d}Q_j}{\mathrm{d}y} = F_4 \tag{16}$$

where z_{ij} stands for the ith component of vector $\boldsymbol{z}_j$. One can derive the relations

$$z_{3j}\frac{\mathrm{d}Q_j}{\mathrm{d}y} = F_3, \qquad \frac{\mathrm{d}F_3}{\mathrm{d}y} = z_{3j}\frac{\mathrm{d}^2 Q_j}{\mathrm{d}y^2} + z_{ij} H_0^{3i}\frac{\mathrm{d}Q_j}{\mathrm{d}y}$$

$$z_{1j}\frac{\mathrm{d}Q_j}{\mathrm{d}y} = 0, \qquad z_{5j}\frac{\mathrm{d}Q_j}{\mathrm{d}y} = 0 \tag{17}$$

Accounting for the nonzero elements of H_0^{3j} only, Eq. (16) can be written as

$$z_{4j}\frac{\mathrm{d}Q_j}{\mathrm{d}y} = \frac{F_4 - L_0^{43} H_0^{33} F_3 - \left[\mathrm{d}\left(L_0^{43} F_3\right)/\mathrm{d}y\right]}{1 + L_0^{43} H_0^{34}} \tag{18}$$

A similar analysis of the second equation

$$z_{2j}\frac{\mathrm{d}Q_j}{\mathrm{d}y} - i\alpha H_3^{23} z_{3j}\frac{\mathrm{d}Q_j}{\mathrm{d}y} = F_2 \tag{19}$$

with $z_{3j}\,\mathrm{d}Q_j/\mathrm{d}y = F_3$ leads to the form

$$z_{2j}\frac{\mathrm{d}Q_j}{\mathrm{d}y} = F_2 + i\alpha H_3^{23} F_3 \tag{20}$$

Thus, we can rewrite the nonhomogeneous system (15) as

$$\boldsymbol{Z}\frac{\mathrm{d}\boldsymbol{Q}}{\mathrm{d}y} = \varphi, \qquad \varphi_1 = 0$$

$$\varphi_2 = -(H_{10}\boldsymbol{A}_{0\alpha})_2 - i\alpha H_3^{23}(H_{10}\boldsymbol{A}_{0\alpha})_3, \qquad \varphi_3 = -(H_{10}\boldsymbol{A}_{0\alpha})_3$$

$$\varphi_4 = \left\{-(H_{10}\boldsymbol{A}_{0\alpha})_4 + L_0^{43} H_0^{33} F_3 (H_{10}\boldsymbol{A}_{0\alpha})_3 + \frac{\mathrm{d}\left[L_0^{43}(H_{10}\boldsymbol{A}_{0\alpha})_3\right]}{\mathrm{d}y}\right\}\frac{1}{1 + L_0^{43} H_0^{34}}$$

$$\varphi_5 = 0, \qquad \varphi_6 = -(H_{10}\boldsymbol{A}_{0\alpha})_5 \tag{21}$$

A formal solution of Eq. (21) is expressed in the form

$$\boldsymbol{A}_{p\alpha} = \sum_{j=1}^{6}\left(a_j + \int_{y_j}^{y}\frac{D_j}{W}\,\mathrm{d}y\right)\boldsymbol{z}_j \tag{22a}$$

$$W = \det(\boldsymbol{Z}), \qquad \frac{D_j}{W} = \frac{\mathrm{d}Q_j}{\mathrm{d}y} \tag{22b}$$

where the constants a_j and y_j are obtained from the boundary conditions at $y = 0$ and ∞. The function $W(y)$ is given by the equation

$$W(y) = W(\infty)\exp\left[\int_{\infty}^{y} \boldsymbol{tr}(H_0)\,\mathrm{d}y\right] \tag{23}$$

where $W(\infty)$ can be evaluated with known asymptotic relations for the fundamental solutions outside the boundary layer. Summarizing, we obtain

$$\boldsymbol{A}_{p\alpha} = \left(a_1 + \int_0^y \frac{D_1}{W}\,\mathrm{d}y\right)z_1 + \int_\infty^y \frac{D_2}{W}\,\mathrm{d}y\, z_2 + \left(a_3 + \int_0^y \frac{D_3}{W}\,\mathrm{d}y\right)z_3 + \int_\infty^y \frac{D_4}{W}\,\mathrm{d}y\, z_4 + \left(a_5 + \int_0^y \frac{D_5}{W}\,\mathrm{d}y\right)z_5 + \int_\infty^y \frac{D_6}{W}\,\mathrm{d}y\, z_6 \tag{24a}$$

$$a_1 = \frac{c_2E_{235} + c_4E_{435} + c_6E_{635}}{E_{135}} \tag{24b}$$

$$a_3 = \frac{c_2E_{125} + c_4E_{145} + c_6E_{165}}{E_{135}} \tag{24c}$$

$$a_5 = \frac{c_2E_{132} + c_4E_{134} + c_6E_{136}}{E_{135}} \tag{24d}$$

$$c_j = \int_0^\infty \frac{D_j}{W}\,\mathrm{d}y \tag{24e}$$

$$E_{ijk} = \det\begin{Vmatrix} z_{1i} & z_{1j} & z_{1k} \\ z_{3i} & z_{3j} & z_{3k} \\ z_{5i} & z_{5j} & z_{5k} \end{Vmatrix}_{y=0} \tag{24f}$$

where z_{ij} denotes the ith component of the jth vector.

Inverse Laplace Transform

The inverse Laplace transform of Eq. (24a)

$$\boldsymbol{A}_\alpha(y,t;\alpha) = \frac{1}{2\pi i}\int_{p_0-i\infty}^{p_0+i\infty} \boldsymbol{A}_{p\alpha}(y;p,\alpha)e^{pt}\,\mathrm{d}p \tag{25}$$

is determined by the poles (relevant to the discrete spectrum) and branch cuts (relevant to the continuous spectrum) in the complex plane p. Integrating along the contour schematically shown in Fig. 1, we can express Eq. (25) as a sum of integrals along the sides γ^- and γ^+ of each branch cut and a sum of residues associated with the poles that result from the equation $E_{135}(p) = 0$, that is,

$$\boldsymbol{A}_\alpha = \frac{1}{2\pi i}\sum_m \left(\int_{\gamma_m^+} + \int_{\gamma_m^-} \boldsymbol{A}_{p\alpha}e^{pt}\,\mathrm{d}p\right) + \sum_n \mathrm{Res}_n\left(\boldsymbol{A}_{p\alpha}e^{pt}\right) \tag{26}$$

Continuous Spectrum

Solutions of the continuous spectrum correspond to the case where a characteristic number λ_j given by Eq. (11) is purely imaginary, that is, $\lambda_j^2 = -k^2$, $k > 0$, $j = 1, \ldots, 6$. A temporal analysis of the continuous spectrum (the wave number α is a real parameter, and the angular frequency $\omega = ip$ is a complex eigenvalue) was carried out by Grosch and Salwen[24] and Ashpis and Erlebacher[25] for incompressible and compressible boundary layers, respectively.

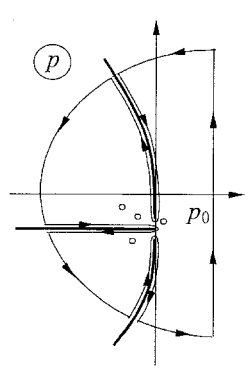

Fig. 1 Integration contour for the inverse Laplace transform.

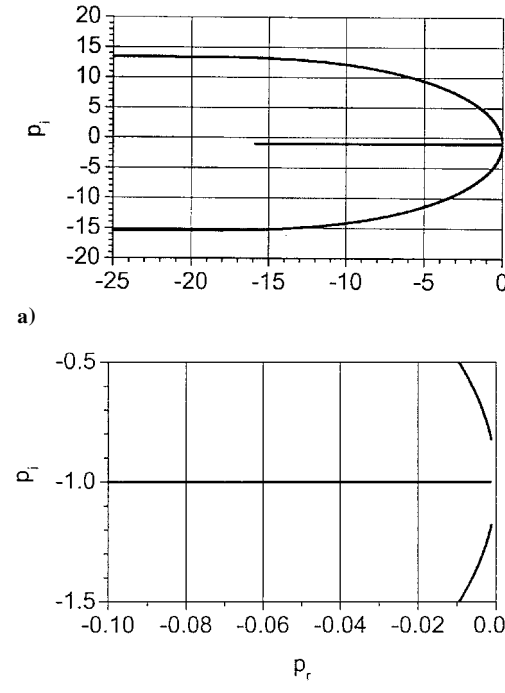

Fig. 2 Three branches of the continuous spectrum in the complex plane p: $M_e = 5.6$, $\alpha = 1$, $\gamma = 1.4$, $Pr = 0.7$, and $Re = 1000$; a) ——, global picture and b) ——, local behavior near the point $p = 0$.

Spatial analyses (ω is a real parameter, and α is a complex eigenvalue) were performed by Salwen and Grosch[26] and Zhigulev et al.[27] for an incompressible boundary layer, and by Tumin and Fedorov[23] (see also Zhigulev and Tumin[28]) and Balakumar and Malik[29] for a compressible boundary layer. We shall recapitulate the main results of the analysis reported in Ref. 25.

The first pure oscillatory solution corresponds to $\lambda_{1,2}^2 = -k^2$ and leads to the relation

$$p_{c,1} = -i\alpha - (k^2 + \alpha^2)/Re \tag{27}$$

This solution is interpreted as a vorticity branch. The equation

$$\left[\left(b_{22} - \lambda^2\right)\left(b_{33} - \lambda^2\right) - b_{23}b_{32}\right] = 0 \tag{28}$$

is a third-order polynomial with respect to p. It has three roots at $\lambda^2 = -k^2$. A numerical evaluation of these roots was performed with the help of *Mathematica*,[30] and the results are shown in Fig. 2 for $M_e = 5.6$, $\alpha = 1$, $\gamma = 1.4$, $Pr = 0.7$, and $Re = 1000$. One branch (the horizontal line) has a finite limiting point, and two others extend to infinity.[25] The horizontal branch is associated with entropy freestream disturbances. [The branch (27) is not shown because it overlaps the entropy branch.] The upper and lower branches are relevant to acoustic waves. They start from the branch points $p = -i\alpha(1 \mp 1/M_e)$, which correspond to the disturbance phase speed $c = 1 \mp 1/M_e$ (slow and fast acoustic waves, respectively).

We denote one side of the branch cuts as "+" and the other as "−" in accordance with the asymptotic behavior:

$$z_-^+ \sim e^{\lambda_1 y}, \quad z_1^- \sim e^{\lambda_1 y}, \quad z_2^+ \sim e^{\lambda_2 y} \tag{29a}$$

$$z_2^- \sim e^{\lambda_2 y}, \quad z_3^+ \sim e^{iky}, \quad z_3^- \sim e^{-iky} \tag{29b}$$

$$z_4^+ \sim e^{-iky}, \quad z_4^- \sim e^{iky}, \quad z_5^+ \sim e^{\lambda_5 y} \tag{29c}$$

$$z_5^- \sim e^{\lambda_5 y}, \quad z_6^+ \sim e^{\lambda_6 y}, \quad z_6^- \sim e^{\lambda_6 y} \tag{29d}$$

where k is real and positive parameter. Then, one can obtain the relations

$$z_1^- = z_1^+, \quad z_2^- = z_2^+, \quad z_3^- = z_4^+ \tag{30a}$$

$$z_4^- = z_3^+, \quad z_5^- = z_5^+, \quad z_6^- = z_6^+ \tag{30b}$$

$$W^+ = -W^-, \qquad D_1^- = -D_1^+, \qquad D_2^- = -D_2^+ \tag{30c}$$

$$D_3^- = -D_4^+, \qquad D_4^- = -D_3^+$$

$$D_5^- = -D_5^+, \qquad D_6^- = -D_6^+ \tag{30d}$$

The integrals along the branch-cut sides $\gamma^\pm$ can be written as one integral of the difference:

$$\begin{aligned}\boldsymbol{A}_{p\alpha}^+ - \boldsymbol{A}_{p\alpha}^- = &\left(a_1^+ + \underline{\int_0^y \frac{D_1^+}{W^+}\,\mathrm{d}y}\right)z_1^+ + \underline{\int_\infty^y \frac{D_2^+}{W^+}\,\mathrm{d}y\, z_2^+} \\ &+ \left(a_3^+ + \int_0^y \frac{D_3^+}{W^+}\,\mathrm{d}y\right)z_3^+ + \int_\infty^y \frac{D_4^+}{W^+}\,\mathrm{d}y\, z_4^+ \\ &+ \left(a_5^+ + \underline{\int_0^y \frac{D_5^+}{W^+}\,\mathrm{d}y}\right)z_5^+ + \underline{\int_\infty^y \frac{D_6^+}{W^+}\,\mathrm{d}y\, z_6^+} \\ &- \left(a_1^- + \underline{\int_0^y \frac{D_1^-}{W^-}\,\mathrm{d}y}\right)z_1^- - \underline{\int_\infty^y \frac{D_2^-}{W^-}\,\mathrm{d}y\, z_2^-} \\ &- \left(a_3^- + \int_0^y \frac{D_3^-}{W^-}\,\mathrm{d}y\right)z_3^- - \int_\infty^y \frac{D_4^-}{W^-}\,\mathrm{d}y\, z_4^- \\ &- \left(a_5^- + \underline{\int_0^y \frac{D_5^-}{W^-}\,\mathrm{d}y}\right)z_5^- - \underline{\int_\infty^y \frac{D_6^-}{W^-}\,\mathrm{d}y\, z_6^-}\end{aligned} \tag{31}$$

Because the underlined terms are canceled, we obtain

$$\begin{aligned}\boldsymbol{A}_{p\alpha}^+ - \boldsymbol{A}_{p\alpha}^- = &\left(a_1^+ - a_1^-\right)z_1^+ + \left(a_3^+ + c_3^+\right)z_3^+ \\ &- \left(a_3^- + c_4^+\right)z_4^+ + \left(a_5^+ - a_5^-\right)z_5^+\end{aligned} \tag{32}$$

Solutions for acoustic waves include four fundamental vector functions. Two of them decay outside the boundary layer, and two others oscillate as $e^{\pm iky}$. Accounting for Eqs. (24a–24f), Eq. (32) can be written in terms of the functions on the + side as

$$\begin{aligned}\boldsymbol{A}_{p\alpha}^+ - \boldsymbol{A}_{p\alpha}^- = &\frac{c_2E_{125} + c_3E_{135} + c_4E_{145} + c_6E_{165}}{E_{145}E_{135}} \\ &\times [-E_{345}z_1 + E_{145}z_3 - E_{135}z_4 + E_{134}z_5]\end{aligned} \tag{33}$$

The vorticity disturbance outside the overlapping region can be expressed in a similar way. It includes two decaying and two oscillating fundamental vectors. An uncertainty exists at the overlapping points, where there are four oscillating and one decaying fundamental solutions, that is, the number of fundamental solutions is larger than is necessary to satisfy the boundary conditions. Analysis of the general solution (24) helps to resolve the difficulty. Because this issue has not been addressed elsewhere, it needs to be discussed in detail.

In the overlapping zone, we denote one side of the branch cut as "+" and the other as "−" and choose the notation of fundamental vectors in accordance with the asymptotic behavior:

$$z_1^+ \sim e^{iky}, \qquad z_1^- \sim e^{-iky}, \qquad z_2^+ \sim e^{-iky} \tag{34a}$$

$$z_2^- \sim e^{iky}, \qquad z_3^+ \sim e^{\lambda_3 y}, \qquad z_3^- \sim e^{\lambda_3 y} \tag{34b}$$

$$z_4^+ \sim e^{\lambda_4 y}, \qquad z_4^- \sim e^{\lambda_4 y}, \qquad z_5^+ \sim e^{ik_1 y} \tag{34c}$$

$$z_5^- \sim e^{-ik_1 y}, \qquad z_6^+ \sim e^{-ik_1 y}, \qquad z_6^- \sim e^{-ik_1 y} \tag{34d}$$

where k and k_1 are real and positive parameters and $\lambda_{3,4}$ are given by Eq. (11b). Then, similar to Eq. (30) one can obtain the relations

$$z_1^- = z_2^+, \qquad z_2^- = z_1^+, \qquad z_3^- = z_3^+ \tag{35a}$$

$$z_4^- = z_4^+, \qquad z_5^- = z_6^+, \qquad z_6^- = z_5^+ \tag{35b}$$

$$W^+ = W^-, \qquad D_1^- = D_2^+, \qquad D_2^- = D_1^+ \tag{35c}$$

$$D_3^- = D_3^+, \qquad D_4^- = D_4^+, \qquad D_5^- = D_6^+, \qquad D_6^- = D_5^+ \tag{35d}$$

The integrals along the branch-cut sides $\gamma^\pm$ can be written as one integral of the difference:

$$\begin{aligned}\boldsymbol{A}_{p\alpha}^+ - \boldsymbol{A}_{p\alpha}^- = &\left(a_1^+ + \int_0^y \frac{D_1^+}{W^+}\,\mathrm{d}y\right)z_1^+ + \int_\infty^y \frac{D_2^+}{W^+}\,\mathrm{d}y\, z_2^+ \\ &+ \left(a_3^+ + \underline{\int_0^y \frac{D_3^+}{W^+}\,\mathrm{d}y}\right)z_3^+ + \underline{\int_\infty^y \frac{D_4^+}{W^+}\,\mathrm{d}y\, z_4^+} \\ &+ \left(a_5^+ + \int_0^y \frac{D_5^+}{W^+}\,\mathrm{d}y\right)z_5^+ + \int_\infty^y \frac{D_6^+}{W^+}\,\mathrm{d}y\, z_6^+ \\ &- \left(a_1^- + \int_0^y \frac{D_1^-}{W^-}\,\mathrm{d}y\right)z_1^- - \int_\infty^y \frac{D_2^-}{W^-}\,\mathrm{d}y\, z_2^- \\ &- \left(a_3^- + \underline{\int_0^y \frac{D_3^-}{W^-}\,\mathrm{d}y}\right)z_3^- - \underline{\int_\infty^y \frac{D_4^-}{W^-}\,\mathrm{d}y\, z_4^-} \\ &- \left(a_5^- + \int_0^y \frac{D_5^-}{W^-}\,\mathrm{d}y\right)z_5^- - \int_\infty^y \frac{D_6^-}{W^-}\,\mathrm{d}y\, z_6^-\end{aligned} \tag{36}$$

Because the underlined terms are canceled, we obtain

$$\begin{aligned}\boldsymbol{A}_{p\alpha}^+ - \boldsymbol{A}_{p\alpha}^- = &\left(a_1^+ + c_1^+\right)z_1^+ + \left(a_3^+ - a_3^-\right)z_3^+ + \left(a_5^+ + c_5^+\right)z_5^+ \\ &- \left(a_1^- + c_2^+\right)z_2^+ - \left(a_5^- + c_6^+\right)z_6^+\end{aligned} \tag{37}$$

Equation (37) can be expressed in the compact explicit form

$$\boldsymbol{A}_{p\alpha}^+ - \boldsymbol{A}_{p\alpha}^- = \boldsymbol{A}_{c,1} + \boldsymbol{A}_{c,2} \tag{38a}$$

$$\begin{aligned}\boldsymbol{A}_{c,1} = &\frac{c_1E_{135} + c_2E_{235} + c_4E_{435} + c_6E_{635}}{E_{135}E_{235}} \\ &\times [E_{235}z_1 - E_{135}z_2 + E_{125}z_3 + E_{132}z_5]\end{aligned} \tag{38b}$$

$$\begin{aligned}\boldsymbol{A}_{c,2} = &\frac{c_1E_{231} + c_4E_{234} + c_5E_{235} + c_6E_{236}}{E_{235}E_{236}} \\ &\times [E_{356}z_2 - E_{256}z_3 + E_{236}z_5 - E_{235}z_6]\end{aligned} \tag{38c}$$

Each term in Eq. (38a) satisfies the boundary condition on the wall and can be interpreted as a stand-alone mode. The first term $\boldsymbol{A}_{c,1}$ represents the vorticity wave with $z_5 \sim e^{ik_1 y}$, and the second term $\boldsymbol{A}_{c,2}$ represents the entropy wave with $z_2 \sim e^{iky}$. Equations (38b) and (38c) also specify weights of vorticity and entropy disturbances in the fundamental solution relevant to the overlapping zone.

Hereafter, we consider the boundary layer over an adiabatic sharp cone at a zero angle of attack. The boundary-layer profiles correspond to the compressible flat-plate boundary-layer solution with the Mangler transformation from a planar to a conical configuration. It is assumed that the distance from the cone tip is so large that nonparallel effects associated with the transverse curvature and the boundary-layer growth can be neglected. The length scale is defined as $L^* = \sqrt{(\mu_e^* x^*/\rho_e^* U_e^*)}$, and the Reynolds number is $Re = \sqrt{(\rho_e^* U_e^* x^*/\mu_e^*)}$. All numerical results are obtained for the local Mach number $M_e = 5.6$, the Reynolds number $Re = 1219.5$, and the stagnation temperature $T_0 = 470$ K. These parameters are chosen to fit the experimental conditions of the Mach-6 Ludwieg tube.[2,3] For this Reynolds number the bow shock effect associated with a hypersonic viscous-inviscid interaction can be neglected because the interaction parameter $\chi = M_e^3/Re \approx 0.14$ is small.[31]

Details of the numerical method are described in Appendix B. Similar analyses can be performed for boundary layers on different conical and planar configurations. Basic features of the disturbance spectrum and the results discussed hereafter are qualitatively the same for a wide class of quasi-parallel flows in presence of streamwise pressure gradient.

The streamwise velocity of the acoustic disturbance is shown in Fig. 3. It is seen that acoustic waves effectively penetrate the

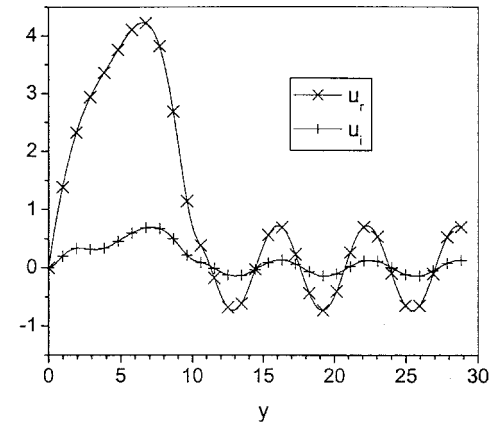

$C < 1 - 1/M_e$

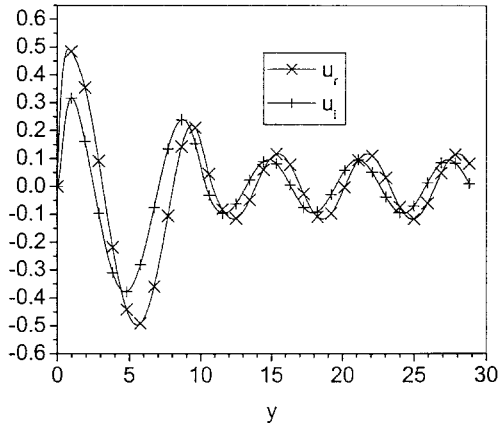

$C > 1 + 1/M_e$

Fig. 3 Streamwise velocity disturbance of the acoustic modes: M_e = 5.6, Re = 1219.5, α = 0.215, and k = 1.

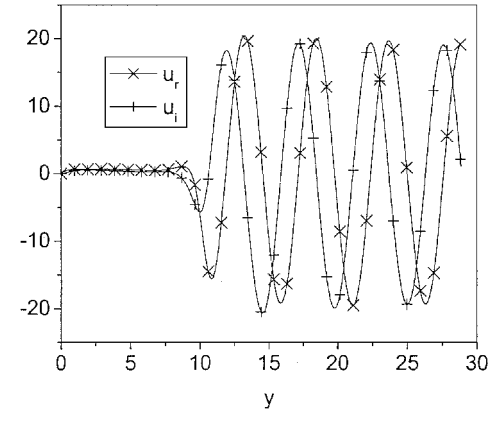

Fig. 4 Streamwise velocity disturbance of the entropy mode: M_e = 5.6, Re = 1219.5, α = 0.215, and k = 1.

boundary layer (the upper boundary-layer edge is $y \approx 10$) and induce velocity oscillations of an amplitude four times larger than that in the outer flow. Figures 4 and 5 show typical distributions of the streamwise velocity disturbance for entropy and vorticity waves, respectively. In contrast to the acoustic waves shown in Fig. 3, the amplitudes of entropy and vorticity waves are almost zero inside the boundary layer. This is consistent with the well-known fact that vortices and temperature spots propagate along the mean-flow streamlines displaced to the outer inviscid flow by the boundary layer. The vorticity/entropy disturbances penetrate the boundary layer as a result of viscous and thermal diffusions, which are weak at the high Reynolds numbers considered herein.

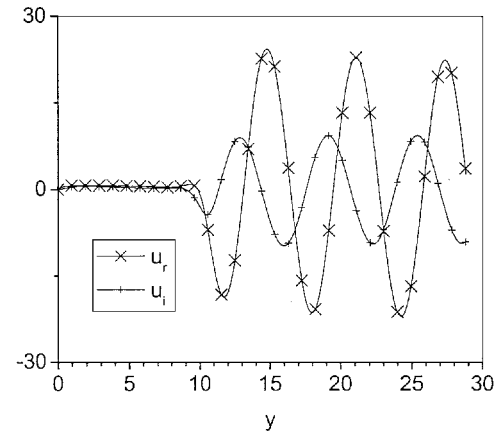

Fig. 5 Streamwise velocity disturbance of the vorticity mode: M_e = 5.6, Re = 1219.5, α = 0.215, and k = 1.

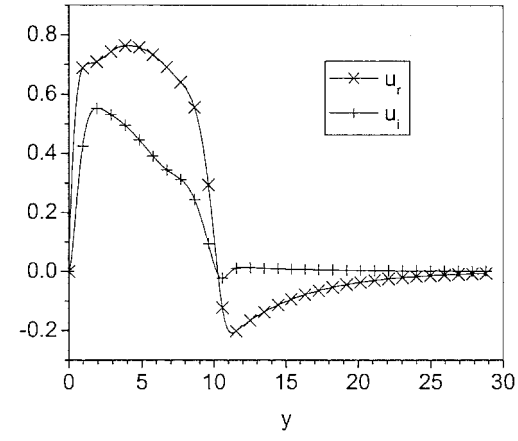

Fig. 6 Streamwise velocity disturbance of the first mode: M_e = 5.6, Re = 1219.5, and α = 0.215.

Discrete Spectrum

The discrete modes are given by the residues of Eq. (26) and correspond to the case where all roots of Eq. (11) have nonzero real parts. These modes are associated with roots of the equation

$$E_{135}(p) = 0 \tag{39}$$

where E_{135} is given by Eq. (24f). The residues are expressed in the form

$$\mathrm{Res}_n\left(\boldsymbol{A}_{p\alpha} e^{pt}\right) = \boldsymbol{A}_n(y; p_n, \alpha) e^{p_n t} \tag{40a}$$

$$\boldsymbol{A}_n = [(c_2 E_{235} + c_4 E_{435} + c_6 E_{635})\boldsymbol{z}_1 + (c_2 E_{125} + c_4 E_{145} + c_6 E_{165})\boldsymbol{z}_3 + (c_2 E_{132} + c_4 E_{143} + c_6 E_{136})\boldsymbol{z}_5]\left[\frac{\partial E_{135}}{\partial p}(p_n)\right]^{-1} \tag{40b}$$

If the eigenvalue p_n does not belong to any of the continuous spectrum branch cuts, then the corresponding function $\boldsymbol{A}_n(y; p_n, \alpha)$ exponentially decays outside the boundary layer, $y \to \infty$. As an example, Fig. 6 shows the streamwise velocity distribution of the first mode for $\alpha = 0.215$.

Summary

Summarizing, we can express the inverse Laplace transform as

$$\boldsymbol{A}_\alpha(y, t; \alpha) = \sum_n \boldsymbol{A}_n(y; p_n, \alpha) e^{p_n t} - \frac{1}{2\pi i} \sum_{m=1}^{4} \int_0^\infty \boldsymbol{A}_{c,m}(y; k, \alpha) e^{p_{c,m}(k) t} \frac{\mathrm{d}p_{c,m}}{\mathrm{d}k} \mathrm{d}k \tag{41}$$

where p_n is a root of Eq. (39) and $\boldsymbol{A}_n$ is given by Eq. (40b); $m = 1$ corresponds to the vorticity wave, with $p_{c,1}$ and $\boldsymbol{A}_{c,1}$ given by Eqs. (27)

and (38b), respectively; $m = 2$ corresponds to the entropy wave, with $p_{c,2}$ and $\boldsymbol{A}_{c,2}$ results of Eqs. (28) and (38c), respectively; and $m = 3, 4$ relate to slow and fast acoustic waves. A numerical evaluation of Eq. (41) is straightforward if there is no coalescing between the discrete and continuous spectra, that is, $p_n \neq p_{c,m}$. However, this is not typical for hypersonic boundary layers. In the next section we show that the first discrete mode is synchronized with the vorticity/entropy waves at a certain wave number $\alpha = \alpha_*$. In the vicinity of this synchronism point, the inverse Laplace transform should be modified as discussed in the next section.

Synchronization of the First Mode with Vorticity/Entropy Waves

We focus on the first and second modes, which are associated with unstable disturbances and play an important role in the initial phase of laminar-turbulent transition. Figure 7 shows numerical results for eigenvalues $\omega_n = ip_n$ of the first ($n = 1$) and second ($n = 2$) modes.

Hereafter the first (second) mode has the phase speed $c_r \to 1 - 1/M_e$ ($c_r \to 1 + 1/M_e$) as $\alpha \to 0$. This terminology is different from that introduced by Mack[4] to describe the multiplicity of inflectional neutral modes. Unfortunately Mack's terminology becomes ambiguous when applied to nonneutral solutions. This motivated us to identify the boundary-layer modes using their asymptotic behavior in the long wavelength limit.

Figure 7 shows that there is a synchronism between the first mode and the entropy and vorticity modes of the phase speed $c = 1$, that is, the eigenvalue ω_1 coincides with the corresponding values of the vorticity/entropy waves at the wave number $\alpha_* \approx 0.19$. The streamwise

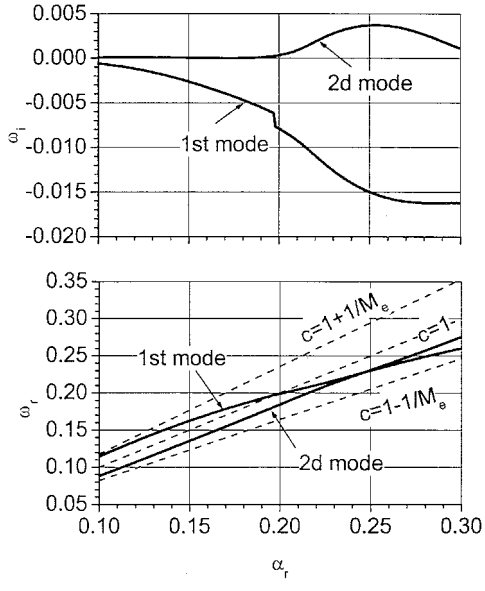

Fig. 7 Numerical evaluation of eigenvalues for the first and second modes: M_e = 5.6, Re = 1219.5, and T_0 = 470 K.

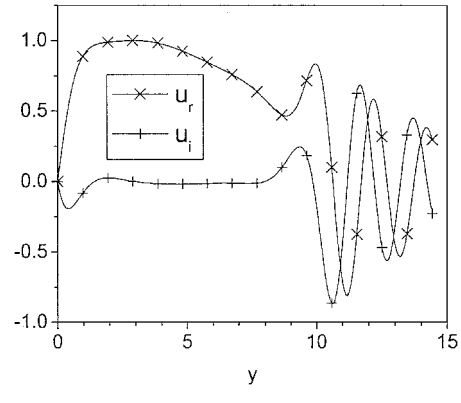

Fig. 8 Streamwise velocity disturbance of the first mode: M_e = 5.6, Re = 1219.5, and α = 0.2.

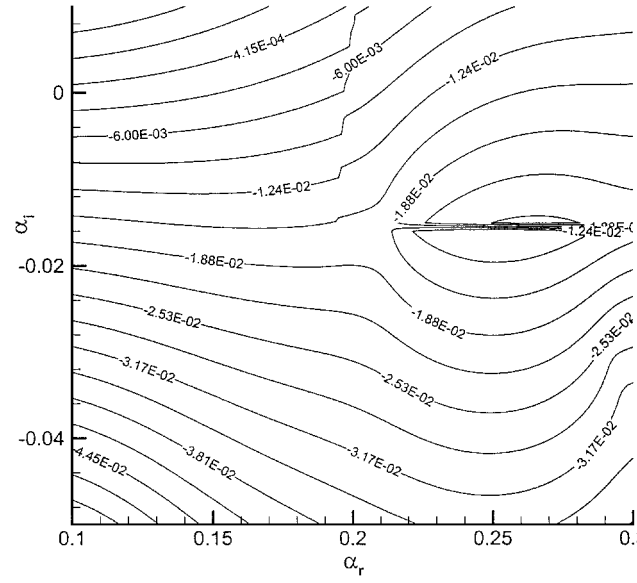

Fig. 9 Contours of ω_i in the complex plane α.

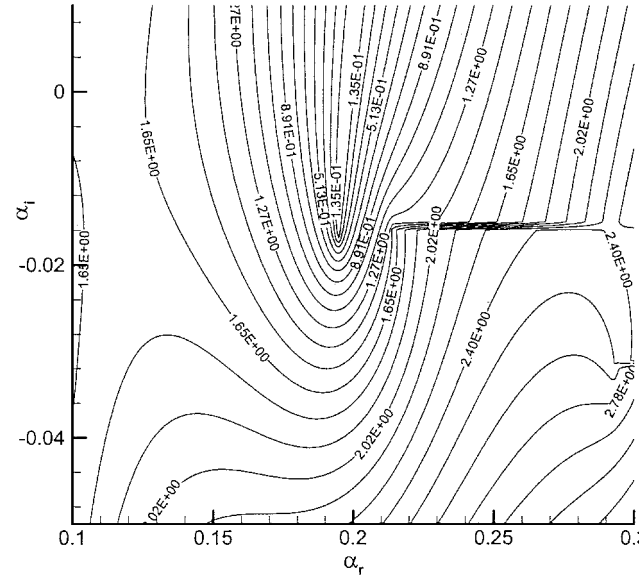

Fig. 10 Contours of $|\mathrm{Re}\lambda_1|$ in the complex plane α.

velocity profile of the first mode at $\alpha = 0.2$ is shown in Fig. 8. In the synchronism vicinity the eigenfunction decays very slowly outside the boundary layer and oscillates similar to the vorticity/entropy waves. As the discrete mode coalesces with the continuous spectrum from one side of the branch cut, it reappears on its other side at another point. This topology leads to a jump of the imaginary part ω_i, shown in Fig. 7. Contours of ω_i in the complex α plane (Fig. 9) indicate that jumps of ω_i are observed along an almost vertical line, starting from the point $\alpha \approx 0.19 - i0.02$. Contours of $|\mathrm{Re}\lambda_1|$ for the first mode in the complex α plane (Fig. 10) show that the discontinuity of ω_i is indeed associated with the coalescing of the first mode with the entropy/vorticity waves ($\mathrm{Re}\lambda_1 = 0$). Note that a similar topology of the disturbance spectrum was reported by Fedorov and Khokhlov[18] regarding the spatial eigenvalues α. They assumed that, in the synchronism region, the vorticity and entropy waves can effectively generate the first mode. Using discretization of the continuous spectrum, they showed that the vorticity/entropy waves translate to the first mode in the vicinity of the synchronism point.

Figure 9 also shows that there is another irregularity at the point $\alpha \approx 0.21 - i0.016$. To illuminate more details of the discontinuity, we plot ω_i vs α_r at different α_i in Fig. 11. This behavior of the growth rate is typical for the branching of two modes. In the present case we deal with branching of the first and second modes that occurs at

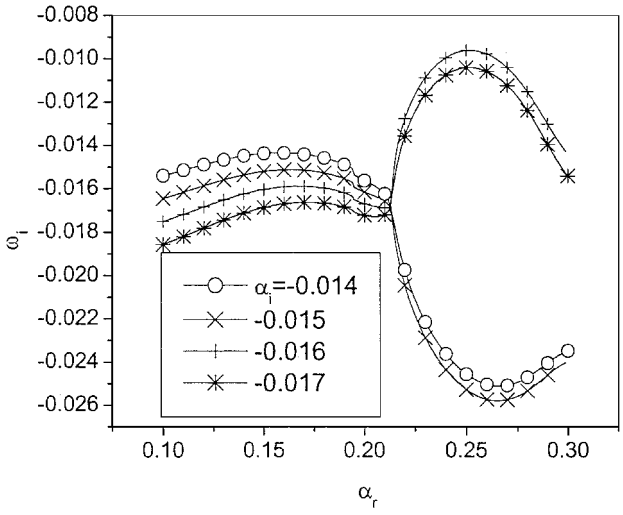

Fig. 11 Plot of ω_i in the vicinity of $\alpha_i = -0.0155$.

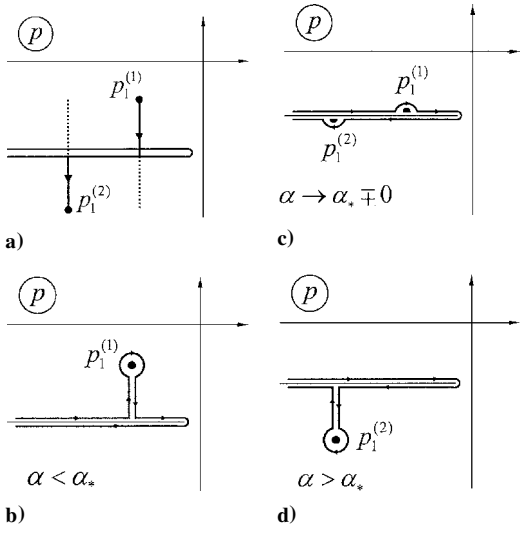

Fig. 12 Spectrum topology and integration contour in the synchronism region.

a complex α. The branching topology is consistent with the results presented in Refs. 16–18. Fedorov and Khokhlov[17,18] investigated an interaction between the first and second modes in the branch-point vicinity as a result of nonparallel effects. They revealed a strong intermodal exchange leading to effective excitation of the second mode instability.

The coalescing of the first mode with the vorticity/entropy waves leads to a nonanalytic behavior of $p_1(\alpha) = i\omega_1(\alpha)$ that might impact an integration path of the inverse Fourier transform and affect both excitation and downstream evolution of the wave packet. This issue was briefly discussed by Reutov and Rybushkina[32] in connection with the wave packet of vortical disturbances propagating in incompressible flow over a flat plate. To resolve this difficulty, we consider the spectrum behavior near the synchronism point. The jump of ω_i at $\alpha = \alpha_*$ indicates that there are two poles $p_1^{(1)}$ and $p_1^{(2)}$ associated with the first mode. Their trajectories in the plane p are schematically shown in Fig. 12a. For $\alpha < \alpha_*$ the pole $p_1^{(1)}$ is above the vorticity/entropy branch cut, and the pole $p_1^{(2)}$ is on the lower sheet of the Riemann surface. The pole $p_1^{(1)}$ approaches the upper side of the branch cut as $\alpha \to \alpha_* - 0$ and eventually disappears on the upper sheet of the Riemann surface when $\alpha > \alpha_*$, whereas the pole $p_1^{(2)}$ approaches the lower side of the branch cut and appears on the plane p when $\alpha > \alpha_*$. A part of the integration contour associated with this spectrum topology can be replaced by the contours schematically shown in Fig. 12b for $\alpha < \alpha_*$ and Fig. 12d for $\alpha > \alpha_*$. Apparently the integrals along the new contours equal the corresponding integrals along the old contour shown in Fig. 1. The former are expressed as

$$\boldsymbol{J}^{(-)} \equiv \boldsymbol{A}_1\left(y;\, p_1^{(1)}, \alpha\right) e^{p_1^{(1)} t} - \frac{1}{2\pi i} \sum_{m=1}^{2} \int_0^{\infty} \boldsymbol{A}_{c,m}(y;\, k, \alpha) \times e^{p_{c,m}(k) t} \frac{\mathrm{d}p_{c,m}}{\mathrm{d}k}\, \mathrm{d}k, \qquad \alpha < \alpha_* \tag{42a}$$

$$\boldsymbol{J}^{(+)} \equiv \boldsymbol{A}_1\left(y;\, p_1^{(2)}, \alpha\right) e^{p_1^{(2)} t} - \frac{1}{2\pi i} \sum_{m=1}^{2} \int_0^{\infty} \boldsymbol{A}_{c,m}(y;\, k, \alpha) \times e^{p_{c,m}(k) t} \frac{\mathrm{d}p_{c,m}}{\mathrm{d}k}\, \mathrm{d}k, \qquad \alpha > \alpha_* \tag{42b}$$

The lower limit $\alpha \to \alpha_* - 0$ of $\boldsymbol{J}^{(-)}$ equals the upper limit $\alpha \to \alpha_* + 0$ of $\boldsymbol{J}^{(+)}$ and equals the integral along the contour shown in Fig. 12c, that is,

$$\boldsymbol{J}^{(+)}(\alpha_*) = \boldsymbol{J}^{(-)}(\alpha_*) = \frac{1}{2} \sum_{j=1}^{2} \boldsymbol{A}_1\left[y;\, p_1^{(j)}, \alpha\right] e^{p_1^{(j)} t} - \frac{1}{2\pi i} \sum_{m=1}^{2} \mathrm{PV} \int_0^{\infty} \boldsymbol{A}_{c,m}(y;\, k, \alpha) e^{p_{c,m}(k) t} \frac{\mathrm{d}p_{c,m}}{\mathrm{d}k}\, \mathrm{d}k \tag{42c}$$

where PV denotes the principal value of the integral. Summarizing, we conclude that, despite the p_1 jump, the inverse Laplace transform (41) has no discontinuity at the synchronism point α_*. Therefore, the inverse Fourier transform can be performed along the real axis of the complex plane α and expressed as

$$\boldsymbol{A}(x, y, t) = \frac{1}{\sqrt{2\pi}} \int_{-\infty}^{+\infty} \boldsymbol{A}_\alpha(y, t; \alpha) e^{i\alpha x}\, \mathrm{d}\alpha \tag{43}$$

Biorthogonal System of Eigenfunctions

A solution of the initial boundary value problem (41) can also be presented as an expansion in the biorthogonal eigenfunctions system $\{\boldsymbol{A}_\omega, \boldsymbol{B}_\omega\}$, where the vector $\boldsymbol{A}_\omega$ is a solution of the direct problem:

$$\frac{\mathrm{d}}{\mathrm{d}y}\left(L_0 \frac{\mathrm{d}\boldsymbol{A}_\omega}{\mathrm{d}y}\right) + \frac{\mathrm{d}\boldsymbol{A}_\omega}{\mathrm{d}y} = -i\omega H_{10} \boldsymbol{A}_\omega + H_{11} \boldsymbol{A}_\omega + i\alpha H_2 \boldsymbol{A}_\omega + i\alpha H_3 \frac{\mathrm{d}\boldsymbol{A}_\omega}{\mathrm{d}y} - \alpha^2 H_4 \boldsymbol{A}_\omega \tag{44a}$$

$$y = 0: \qquad A_{\omega 1} = A_{\omega 3} = A_{\omega 5} = 0 \tag{44b}$$

$$y \to \infty: \qquad |A_{\omega j}| < \infty \tag{44c}$$

and the vector $\boldsymbol{B}_\omega$ is a solution of the adjoint problem:

$$\frac{\mathrm{d}}{\mathrm{d}y}\left(L_0^* \frac{\mathrm{d}\boldsymbol{B}_\omega}{\mathrm{d}y}\right) - \frac{\mathrm{d}\boldsymbol{B}_\omega}{\mathrm{d}y} = i\bar{\omega} H_{10}^* + \boldsymbol{B}_\omega H_{11}^* \boldsymbol{B}_\omega - i\alpha H_2^* \boldsymbol{B}_\omega + i\alpha H_3^* \frac{\mathrm{d}\boldsymbol{B}_\omega}{\mathrm{d}y} - \alpha^2 H_4^* \boldsymbol{B}_\omega \tag{45a}$$

$$y = 0: \qquad B_{\omega 2} = B_{\omega 3} = B_{\omega 5} = 0 \tag{45b}$$

$$y \to \infty: \qquad |B_{\omega j}| < \infty \tag{45c}$$

The asterisk in Eqs. (45) denotes a Hermitian adjoint matrix, and the overbar denotes a complex conjugate value. The direct problem (44) can be expressed in the standard form (9). The adjoint problem (45) can also be expressed in a similar form as

$$-\frac{\mathrm{d}\boldsymbol{Y}}{\mathrm{d}y} = H_0^* \boldsymbol{Y} \tag{46a}$$

$$y = 0: \qquad Y_2 = Y_4 = Y_6 = 0 \tag{46b}$$

$$y \to \infty: \qquad |Y_j| < \infty \tag{46c}$$

One can establish correspondence between $\boldsymbol{B}_\omega$ and $\boldsymbol{Y}$. The relationships are presented in Appendix C. The latter were checked with

the help of *Mathematica* software.[30] Solutions of the problems (44) and (45) belong to discrete and continuous spectra. Equations (33), (38), and (40) represent modes satisfying Eqs. (44), with weights depending on the initial data $\boldsymbol{A}_{0\alpha}$.

For the eigenvector system $\{\boldsymbol{A}_\omega, \boldsymbol{B}_\omega\}$ the following orthogonality relation is valid:

$$\langle H_{10}\boldsymbol{A}_\omega, \boldsymbol{B}_{\omega'}\rangle \equiv \int_0^\infty (H_{10}\boldsymbol{A}_\omega, \boldsymbol{B}_{\omega'})\,\mathrm{d}y = \Delta_{\omega,\omega'} \qquad (47)$$

where $\Delta_{\omega,\omega'}$ is the Kronecker symbol if ω or ω' belongs to the discrete spectrum; $\Delta_{\omega,\omega'} = \delta(\omega - \omega')$ is a delta function if both ω and ω' belong to the continuous spectrum. We assume that solutions of the adjoint problem (46) are properly normalized to make the coefficient on the right-hand side of Eq. (47) equal to unity.

Following Refs. 23 and 24, one can analyze the coefficients of the formal solution (33), (38), and (40) and show that the inverse Laplace transform is expressed in the form of expansion into the biorthogonal eigenfunction system

$$\boldsymbol{A}_\alpha(y,t) = \sum_v c_v \boldsymbol{A}_\alpha \omega_v(y) e^{-i\omega_v t} + \sum_j \int_0^\infty c_j(k)\boldsymbol{A}_\alpha \omega_j(y) e^{-i\omega_j(k)t}\,\mathrm{d}k \qquad (48)$$

Here, $\sum_v$ and $\sum_j$ denote the sum over the discrete and continuous spectra, respectively. In Eq. (48) the frequency $\omega = ip$ is used instead of the Laplace variable p. The statement that the inverse Laplace transform (41) can be presented in the form (48) means completeness of the biorthogonal eigenfunction system. The coefficients c_v and c_j can be found from the Fourier transform of the initial data $\boldsymbol{A}_{0\alpha}(y)$, using the orthogonality relation (47). Although a numerical evaluation of the expansion (41) is straightforward, it is more convenient to use the biorthogonal eigenfunction system to determine the weight of each mode. In the next section we will apply this technique for evaluation of boundary-layer receptivity to temperature spottiness.

Receptivity to Temperature Spots

As an example, we consider the initial temperature spot localized at a distance y_0 from the wall, that is,

$$\theta(x, y) = \delta(y - y_0)\delta(x) \qquad \text{at} \qquad t = 0 \qquad (49)$$

The orthogonality condition (47) allows us to determine the weight c_1 of the first-mode wave generated by the temperature spot

$$c_1(\alpha) = \frac{\langle H_{10}A_{0\alpha}, B_\omega\rangle}{\langle H_{10}A_\omega, B_\omega\rangle} \qquad (50)$$

where the frequency $\omega(\alpha)$ corresponds to the first-mode eigenvalue. The denominator $\langle H_{10}A_\omega, B_\omega\rangle$ is included in Eq. (50) for the case of an arbitrary normalization of the adjoint-problem solution. The physical meaning of the coefficient c_1 depends on the normalization of the eigenfunction A_ω. For example, if the eigenfunction is normalized as $u_{\max} = \max[u(y)] = 1$ the coefficient c_1 is the amplitude of the maximum streamwise velocity component $u_{\max}$ associated with the first mode. For a temperature spot of the shape given by Eq. (49), Eq. (50) leads to the expression

$$c_1(\alpha) = \frac{H_{10}^{35}(y_0)B_{3\omega}(y_0) + H_{10}^{65}(y_0)B_{6\omega}(y_0)}{\langle H_{10}A_\omega, B_\omega\rangle} \qquad (51)$$

Figure 13 shows the maximum streamwise velocity amplitude $u_{\max}$ of the first-mode wave, which is generated by α components of the temperature spot localized at various normal distances y_0 from the wall. Figure 14 illustrates the distributions of $u_{\max}(y_0)$ for various fixed wave numbers. These data can be treated as distributions of the receptivity coefficient with respect to α and y_0. It is seen that receptivity is highly nonuniform in the $\alpha - y_0$ space. Long-wave components of the temperature spot (with $\alpha < 0.19$) have almost no effect on the first mode. As expected, the highest receptivity occurs

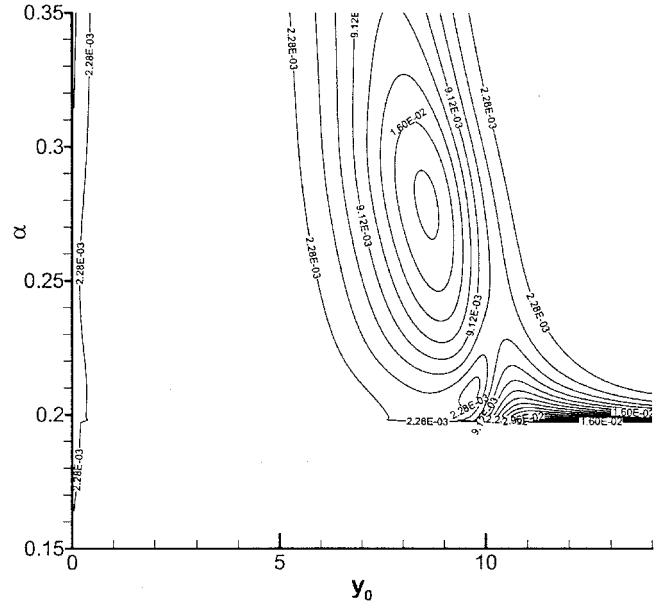

Fig. 13 Map of the streamwise velocity component (first mode) generated by the α component of the temperature spot.

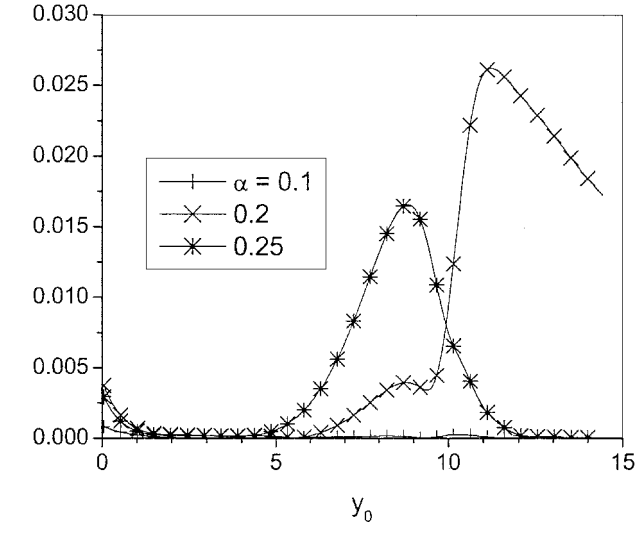

Fig. 14 Amplitude of the streamwise velocity component of the first mode generated by the α component of the temperature spot.

in the vicinity of the synchronism point $\alpha_* \approx 0.2$, where the receptivity coefficient has a sharp peak. The maximum $u_{\max} \approx 0.03$ is observed at the distance $y_0 \approx 11$ close to the upper boundary-layer edge. Its value (as well as the width $\Delta\alpha$) decreases with the distance y_0. However, even at y_0 twice the boundary-layer thickness, the synchronized components of the temperature spot generate the first-mode wave of the appreciable amplitude $u_{\max} \approx 0.01$. This indicates that the boundary-layer flow is highly receptive to the temperature spottiness in the synchronism region where the first-mode phase speed is close to that of the mean-flow speed at the upper boundary-layer edge. Just downstream of this region, the first mode effectively excites the unstable second mode,[17,18] which triggers the initial phase of transition. This scenario might be important in a low-noise environment, when the acoustic component of freestream disturbances is small compared with the temperature spottiness. It might be also important in the case of the low receptivity in the leading-edge region, which is typical for conical configurations.

The second maximum of the receptivity coefficient is located in the vicinity of $\alpha \approx 0.28$ and $y_0 \approx 8.5$. It is observed in the range $5 < y_0 < 11$ and associated with the temperature disturbances initialized inside the boundary layer. Because its width $\Delta\alpha$ is essentially larger than that of the peak as a result of synchronization, the

first-mode wave packet resulting from integration over α might have a relatively large amplitude. However, this mechanism implies the presence of a local forcing source within the boundary layer. Such a source can be induced artificially (for example, using a laser beam); however, it does not occur in natural flows because the freestream temperature spottiness weakly penetrates the boundary layer.

Conclusions

In this paper we analyzed the initial-value problem for two-dimensional disturbances propagating in a hypersonic boundary layer over a sharp cone at a zero angle of attack. It is shown that its solution can be presented as an expansion in the biorthogonal eigenfunction system. This approach provides a compact and robust formalism for theoretical assessments of hypersonic boundary-layer receptivity to freestream disturbances such as temperature spots and vortical perturbations. The analytical and numerical results lead to the following conclusions:

1) The spectrum topology of a hypersonic boundary layer is substantially different from that of the subsonic case. The discrete spectrum reveals a nonanalytic behavior of its dispersion relationship caused by synchronization of the first mode (for an adiabatic wall) or the second mode (for a strongly cooled wall) with the vorticity/entropy waves of the continuous spectrum.

2) In the synchronism region the boundary layer is highly receptive to temperature spottiness and/or freestream turbulence. The receptivity maximum is located near the upper boundary-layer edge, where vortical and temperature disturbances are naturally concentrated as a result of the boundary-layer displacement effect. This receptivity mechanism can play an important role in the initial phase of transition for the case of free flights and "quiet" wind tunnels when the freestream acoustic field is relatively weak. It might be competitive with the leading-edge receptivity, especially for conical configurations with relatively small leading-edge areas.

3) The second maximum of the receptivity coefficient is associated with local disturbances induced inside the boundary layer. A natural occurrence of these disturbances is unlikely; however, they can be generated artificially using a laser beam or spark-discharge techniques. The theoretical predictions can be validated by experiments in quiet wind tunnels. A good candidate for such experiments might be the high-Reynolds-number Mach-6 Ludwieg tube, which is presently being constructed at Purdue University. A laser perturber can be used to induce temperature spots in a freestream and to conduct detailed measurements of receptivity characteristics. The theoretical model discussed in this paper can help in the design of such an experiment and in the interpretation of the data.

Appendix A: Nonzero Elements of the Matrices in Eqs. (2) and (9)

Nonzero elements of the matrices in Eqs. (2b) and (9) are

$$H_{10}^{21} = Re/\mu_s T_s, \qquad H_{10}^{34} = -\gamma M_e^2, \qquad H_{10}^{35} = 1/T_s$$

$$H_{10}^{43} = -1/T_s, \qquad H_{10}^{64} = -(RePr/\mu_s)(\gamma - 1)M_e^2$$

$$H_{10}^{65} = RePr/T_s\mu_s, \qquad H_{11}^{12} = 1, \qquad H_{11}^{23} = (Re/\mu_s T_s)DU_s$$

$$H_{11}^{22} = -D(\ln\mu_s), \qquad H_{11}^{25} = -[D(\mu_s' DU_s)/\mu_s]$$

$$H_{11}^{26} = -(\mu_s'/\mu_s)DU_s, \qquad H_{11}^{56} = 1, \qquad H_{11}^{33} = DT_s/T_s$$

$$H_{11}^{63} = (RePr/T_s\mu_s)DT_s$$

$$H_{11}^{65} = -\left[Pr(\gamma - 1)M_e^2/\mu_s\right]\mu_s'(DU_s)^2 - [D(\mu_s' DT_s)/\mu_s]$$

$$H_{11}^{66} = -2\mu_s' DT_s/\mu_s, \qquad H_{11}^{62} = -2DU_s Pr(\gamma - 1)M_e^2$$

$$H_2^{21} = ReU_s/\mu_s T_s, \qquad H_2^{23} = -D(\ln\mu_s), \qquad H_2^{24} = Re/\mu_s$$

$$H_2^{31} = -1, \qquad H_2^{34} = -\gamma M_e^2 U_s, \qquad H_2^{35} = U_s/T_s$$

$$H_2^{41} = mD\mu_s/Re, \qquad H_2^{42} = (m+1)\mu_s/Re$$

$$H_2^{43} = -U_s/T_s, \qquad H_2^{45} = \mu_s' DS_s/Re$$

$$H_2^{63} = -2PrDU_s(\gamma - 1)M_e^2$$

$$H_2^{64} = -(RePr/\mu_s)(\gamma - 1)M_e^2 U_s, \qquad H_2^{65} = (RePr/T_s\mu_s)U$$

$$H_3^{23} = -(m+1), \qquad H_4^{21} = -r, \qquad H_4^{43} = \mu_s/Re$$

$$H_4^{65} = -1, \qquad L_0^{43} = -r\mu_s/Re, \qquad H_0^{12} = H_0^{56} = 1$$

$$H_0^{21} = \alpha^2 + i(\alpha U_s - ip)Re/\mu_s T_s, \qquad H_0^{22} = -D\mu_s/\mu_s$$

$$H_0^{23} = -i\alpha(m+1)DT_s/T_s - i\alpha D\mu_s/\mu_s + ReDU_s/\mu_s T_s$$

$$H_0^{24} = i\alpha Re/\mu_s - (m+1)\gamma M_e^2\alpha(\alpha U_s - ip)$$

$$H_0^{25} = \alpha(m+1)(\alpha U_s - ip)/T_s - D(\mu_s' DU_s)/\mu_s$$

$$H_0^{26} = -\mu_s' DU_s/\mu_s, \qquad H_0^{31} = -i\alpha, \qquad H_0^{33} = DT_s/T_s$$

$$H_0^{34} = -i\gamma M_e^2(\alpha U_s - ip), \qquad H_0^{35} = i(\alpha U_s - ip)/T_s$$

$$\chi = \left[Re/\mu_s + ir\gamma M_e^2(\alpha U_s - ip)\right]^{-1}$$

$$H_0^{41} = -i\alpha\chi(rDT_s/T_s + 2D\mu_s/\mu_s), \qquad H_0^{42} = -i\alpha\chi$$

$$H_0^{43} = \chi\big[-\alpha^2 - i(\alpha U_s - ip)Re/\mu_s T_s + rD^2 T_s/T_s + rD\mu_s DT_s/\mu_s T_s\big]$$

$$H_0^{44} = -i\chi r\gamma M_e^2[\alpha DU_s + (\alpha U_s - ip)(DT_s/T_s + D\mu_s/\mu_s)]$$

$$H_0^{45} = i\chi[r\alpha DU_s/T_s + \alpha\mu_s' DU_s/\mu_s + r(\alpha U_s - ip)D\mu_s/\mu_s T_s]$$

$$H_0^{46} = ir\chi(\alpha U_s - ip)/T_s, \qquad H_0^{62} = -2(\gamma - 1)M_e^2 PrDU_s$$

$$H_0^{63} = -2i\alpha(\gamma - 1)M_e^2 PrDU_s + RePrDT_s/\mu_s T_s$$

$$H_0^{64} = -iRePr(\gamma - 1)M_e^2(\alpha U_s - ip)/\mu_s$$

$$H_0^{65} = \alpha^2 + iRePr(\alpha U_s - ip)/\mu_s T_s - (\gamma - 1)M_e^2 Pr\mu_s'(DU_s)^2/\mu_s - D^2\mu_s/\mu_s$$

$$H_0^{66} = -2D\mu_s/\mu_s$$

Appendix B: Numerical Method

The conventional forms of Eqs. (9) and (46) for the direct and adjoint problems were used in the numerical evaluations. Afterward, the adjoint eigenfunction $\boldsymbol{B}_\omega$ was found with the help of the relationships from Appendix C. The numerical procedure incorporates the integration of Eqs. (9) and (46) for three (discrete spectrum) or four (continuous spectrum) fundamental solutions. The integration was carried out from outside the boundary layer ($y_{\max} \approx 14$) toward the wall employing the Gram–Schmidt orthonormalization procedure. The integration was fulfilled with a fourth-order Runge–Kutta scheme with a constant step (301 points on the interval).

In the analysis of the discrete spectrum, the complex frequency ω was found using Newton's iteration procedure. The iterations were considered converged if the temperature disturbance on the wall were less than 10^{-5}, whereas u and v were kept equal to zero. In consideration of the continuous spectra, k was used as a parameter, and the frequency ω was found from the equation $\lambda_j^2 = -k^2$ with the help of *Mathematica*.[30]

The inner product $\langle H_{10} A_\omega, B_\omega \rangle$ in Eq. (50) was calculated numerically on the interval $[0, y_{\max}]$ and analytically on the interval $[y_{\max}, \infty]$.

The iteration procedure in the analysis of the discrete spectrum depends on the initial approach to the eigenvalue ω. This dependency might be especially strong in the vicinity of the synchronisms just described. To find the initial approach and to validate the results obtained with the code based on the Runge–Kutta scheme, we developed a code using the two-domain Chebyshev spectral collocation method.[33] To validate the latter code, we reproduced the main results of Refs. 33 and 34.

Appendix C: Correspondence Between Solutions of the Adjoint Problems, Eqs. (45) and (46)

$$B_1 = Y_1 + \frac{i\alpha r Y_4}{\left[Re/\mu_s - ir\gamma M_e^2(\alpha U_s - \bar{\omega})\right]}$$

$$B_2 = Y_2$$

$$B_3 = i\alpha(m+1)Y_2 + Y_3 + \frac{rDT_s}{T_s}\frac{Y_4}{\left[Re/\mu_s - ir\gamma M_e^2(\alpha U_s - \bar{\omega})\right]} - \frac{r\mu_s}{Re}\frac{\mathrm{d}}{\mathrm{d}y}\left(\frac{Y_4}{\left[1 - i(r\mu_s/Re)\gamma M_e^2(\alpha U_s - \bar{\omega})\right]}\right)$$

$$B_4 = Y_4\left\{\frac{1}{\left[1 - i(r\mu_s/Re)\gamma M_e^2(\alpha U_s - \bar{\omega})\right]}\right\}$$

$$B_5 = Y_5 - \frac{ir(\alpha U_s - \bar{\omega})}{T_s}\frac{Y_4}{\left[Re/\mu_s - ir\gamma M_e^2(\alpha U_s - \bar{\omega})\right]}$$

$$B_6 = Y_6$$

Acknowledgments

The authors benefited from valuable comments and suggestions of anonymous reviewers.

References

[1]Reshotko, E., "Boundary Layer Instability, Transition, and Control," AIAA Paper 94-0001, Jan. 1994.

[2]Schneider, S. P., "Design and Fabrication of a 9.5-Inch Mach-6 Quiet-Flow Ludwieg Tube," AIAA Paper 98-2511, June 1998.

[3]Schneider, S. P., "Initial Shakedown of the Purdue Mach-6 Quiet-Flow Ludwieg Tube," AIAA Paper 2000-2592, June 2000.

[4]Mack, L. M., "Boundary-Layer Stability Theory," Jet Propulsion Lab., JPL 900-277, Pasadena, CA, Nov. 1969.

[5]Kendall, J. M., "Wind Tunnel Experiments Relating to Supersonic and Hypersonic Boundary Layer Transition," *AIAA Journal*, Vol. 13, No. 3, 1975, pp. 290–299.

[6]Demetriades, A., "Hypersonic Viscous Flow over a Slender Cone, Part III: Laminar Instability and Transition," AIAA Paper 74-535, Jan. 1974.

[7]Stetson, K. F., Thompson, E. R., Donaldson, J. C., and Siler, L. G., "Laminar Boundary Layer Stability Experiments on a Cone at Mach 8. Part 1: Sharp Cone," AIAA Paper 83-1761, July 1983.

[8]Stetson, K. F., and Kimmel, R. L., "The Hypersonic Boundary Layer Stability," AIAA Paper 92-0737, Jan. 1992.

[9]Simen, M., and Dallman, U., "On the Instability of Hypersonic Flow past a Pointed Cone—Comparison of Theoretical and Experimental Results at Mach 8," Deutscher Luft- und Raumfahrtkongress/DGLR–Jahrestagung, Bremen, Germany, 1992, pp. 31-1–31-13.

[10]Gasperas, G., "Effect of Wall Temperature Distribution on the Stability of Compressible Boundary Layer," AIAA Paper 89-1894, June 1989.

[11]Kendall, J. M., "Supersonic Boundary Layer Stability Experiments," *Proceedings of Boundary Layer Transition Study Group Meeting*, edited by W. D. McCanley, U.S. Air Force Rept. BSD-TR-67-213, Vol. 2, 1967, pp. 10-1–10-8.

[12]Maslov, A. A., Shiplyuk, A. N., Sidorenko, A. A., and Arnal, D., "Leading-Edge Receptivity of a Hypersonic Boundary Layer on a Flat Plate," *Journal of Fluid Mechanics*, Vol. 426, 2001, pp. 73–94.

[13]Kosinov, A. D., Maslov, A. A., and Shevelkov, S. G., "Experiments on the Stability of Supersonic Laminar Boundary Layers," *Journal of Fluid Mechanics*, Vol. 219, 1990, pp. 621–633.

[14]Ladoon, D. W., and Schneider, S. P., "Measurements of Controlled Wave Packets at Mach 4 on a Cone at Angle of Attack," AIAA Paper 98-0436, Jan. 1998.

[15]Schmisseur, J. D., and Schneider, S. P., "Receptivity of the Mach-4 Boundary-Layer on an Elliptic Cone to Laser-Generated Localized Free-Stream Perturbations," AIAA Paper 98-0532, Jan. 1998.

[16]Gushchin, V. R., and Fedorov, A. V., "Excitation and Development of Unstable Disturbances in a Supersonic Boundary Layer," *Fluid Dynamics*, Vol. 25, No. 3, 1990, pp. 344–352.

[17]Fedorov, A. V., and Khokhlov, A. P., "Excitation and Evolution of Unstable Disturbances in Supersonic Boundary Layer," *Proceedings of 1993 ASME Fluid Engineering Conference*, FED-Vol. 151, Transitional and Turbulent Compressible Flows, American Society of Mechanical Engineers, New York, 1993, pp. 1–13.

[18]Fedorov, A. V., and Khokhlov, A. P., "Pre-History of Instability in a Hypersonic Boundary Layer," *Theoretical and Computational Fluid Dynamics*, Vol. 14, No. 6, 2001, pp. 359–375.

[19]Fedorov, A. V., and Khokhlov, A. P., "Excitation of Unstable Modes in a Supersonic Boundary Layer by Acoustic Waves," *Fluid Dynamics*, Vol. 26, No. 4, 1991, pp. 531–537.

[20]Chen, F.-J., Beckwith, I. E., and Creel, T. R., "Effects of Streamwise Variations in Noise Levels and Spectra on Supersonic Boundary-Layer Transition," AIAA Paper 84-0010, Jan. 1984.

[21]McKenzie, J. F., and Westpal, K. O., "Interaction of Linear Waves with Oblique Shock Waves," *Physics of Fluids*, Vol. 11, No. 11, 1968, pp. 2350–2362.

[22]Gustavsson, L. H., "Initial-Value Problem for Boundary Layer Flows," *Physics of Fluids*, Vol. 22, No. 9, 1979, pp. 1602–1605.

[23]Tumin, A. M., and Fedorov, A. V., "Spatial Growth of Disturbances in a Compressible Boundary," *Journal of Applied Mechanics and Technical Physics*, Vol. 24, No. 4, 1983, pp. 548–554.

[24]Grosch, C. E., and Salwen, H., "The Continuous Spectrum of the Orr-Sommerfeld Equation 1. The Spectrum and the Eigenfunctions," *Journal of Fluid Mechanics*, Vol. 87, Pt. 1, 1978, pp. 33–54.

[25]Ashpis, D. E., and Erlebacher, G., "On the Continuous Spectra of the Compressible Boundary Layer Stability Equation," *Instability and Transition, Proceedings of the ICASE/NASA LaRC Workshop*, edited by M. Y. Hussaini and R. G. Voight, Springer-Verlag, New York, 1990, pp. 145–159.

[26]Salwen, H., and Grosch, C. E., "The Continuous Spectrum of the Orr–Sommerfeld Equation, Part 2. Eigenfunction Expansion," *Journal of Fluid Mechanics*, Vol. 104, 1984, pp. 445–465.

[27]Zhigulev, V. N., Sidorenko, N. V., and Tumin, A. M., "Generation of Instability Waves in a Boundary Layer by External Turbulence," *Journal of Applied Mechanics and Technical Physics*, Vol. 21, No. 6, 1980, pp. 28–34.

[28]Zhigulev, V. N., and Tumin, A. M., *Origin of Turbulence*, Nauka, Novosibirsk, Russia, 1987 (in Russian); also NASA TT-20340, Oct. 1988 (translated).

[29]Balakumar, P., and Malik, M. R., "Discrete Modes and Continuous Spectra in Supersonic Boundary Layers," *Journal of Fluid Mechanics*, Vol. 239, 1992, pp. 631–656.

[30]Wolfram, S., *The Mathematica Book*, 4th ed., Wolfram Media and Cambridge Univ. Press, New York, 1999.

[31]Hayes, W. D., and Probstein, R. F., *Hypersonic Flow Theory*, Academic Press, New York, 1959, p. 350.

[32]Reutov, V. N., and Rybushkina, G. V., "Spatial Evolution of Continuous Mode Packets Locally Forced in a Boundary-Layer Flow," *European Journal of Mechanics, B/Fluids*, Vol. 12, No. 4, 1993, pp. 475–492.

[33]Malik, M. R., "Numerical Methods for Hypersonic Boundary Layer Stability," *Journal of Computational Physics*, Vol. 86, 1990, pp. 376–413.

[34]Hanifi, A., Schmid, P. J., and Henningson, D. S., "Transient Growth in Compressible Boundary Layer Flow," *Physics of Fluids*, Vol. 8, 1996, pp. 51–65.

M. Sichel
Associate Editor